Numerical study of nano and micro pollutant particle transport and deposition in realistic human lung airways

Md. M. Rahman [1, 2], Ming Zhao [1, *], Mohammad S. Islam [3], Kejun Dong [4], and Suvash C. Saha [3]

[1] School of Engineering, Design and Built Environment, Western Sydney University, Penrith, NSW 2751, Australia.
[2] Department of Mathematics, Faculty of Science, Islamic University, Kushtia-7003, Bangladesh.
[3] School of Mechanical and Mechatronic Engineering, University of Technology Sydney, Ultimo, NSW 2007, Australia.
[4] Center for Infrastructure Engineering, Western Sydney University, Penrith, NSW 2751, Australia.

***Correspondence author:** m.zhao@westernsydney.edu.au

Abstract

For respiratory health risk assessment, it is essential to evaluate the transportation and deposition (TD) of pollutant particles in human lung airways, which are responsible for lung diseases. Studies to date improved the knowledge of the particle TD in airways. However, the understanding of the TD of different pollutant particles in realistic airways has not been fully understood. This study investigates TD of three types of pollutant particles: traffic, smoke and dust, with various sizes ranging from nano- to micro-scales in the mouth–throat and tracheobronchial lung airways of a human lung using computational fluid dynamics (CFD). Three different physical activities are considered: sleeping, resting, and intense breathing, corresponding to inhalation flow rates of Q_{in}= 15, 30 and 60 L/min, respectively. Nearly 99.8% of 10-µm traffic particles are deposited in the upper lung airways considered here. However, the TD efficiency of 10-µm dust particles is reduced to 64.28% due to the reduction in particle density. Nanoparticles have a much smaller deposition efficiency than microparticles because impaction effect of microparticles is stronger. Only less than 10% of 5-nm traffic particles are deposited in the airways for all three flow rates, allowing over 90% of particles to reach the deep lung. An important finding is that the effects of density on the particle TD of nanoparticles are much weaker than that of microparticles. At 15 L/min flow rate, the difference between the deposition efficiencies of the heaviest traffic particles and the lightest dust particles is only 3.5%. The effects of particle density on the deposition efficiencies of nano- and micro-particles are different from each other because impaction and diffusion dominate the TD of nano- and micro-particles, respectively. Density only affects impaction significantly but has little effect on diffusion.

Keywords: Airflow, Traffic particle, Smoke particle, Dust particle, Human Lungs, Drug delivery, Physical activity, Deposition mechanism

1. Introduction:

Pollutant particles or Particulate matter (PM) of varying sizes, coming from diverse sources, inhaled into human lungs, affect respiratory health globally [1, 2]. PM is a complex mixture of solid and liquid particles suspended in the air that can be carried far distances by the wind. Hazardous PM damages human health after it is inhaled into the human lungs and further enters the blood circulation system [3, 4]. Some of the particles absorbed by epithelial cells can induce respiratory diseases such as asthma, lung cancer, and chronic obstructive pulmonary disease [5, 6]. According to the global burden of disease, air pollution is responsible for 3.1 million premature deaths and 3.2 % of worldwide disability-adjusted life each year [7, 8]. Since 1990, ambient PM has been placed 6th among 79 risk factors in the worldwide burden of human diseases [9].

Because of its huge hazard to human health, pollutant-related particle emission has been a significant source of worry in recent years [10]. The risk is dependent on the size of pollutant particles. Fine particles may pose a significant threat to people because of their potential to penetrate deep into the lungs and lung cell membranes [11, 12], and affect the entire organ system, including the brain [13, 14]. Fine particles have been demonstrated to be more hazardous than larger particles [11, 15].

Large/coarse pollutant particles (2.5-10 μm) produced by crustal material may cause morbidity and mortality [16, 17]. However, they have not been shown to have any substantial negative health impacts in several epidemiological research [18, 19]. However, other studies have discovered that the damage of large pollutant particles on health is much more serious than or at least as powerful as fine pollutants [20, 21].

Diesel and compressed natural gas (CNG) engines create the most ultrafine traffic particles [22]. Most diesel particles are in the 1 nm to 1 μm range [23]. The large surface area of diesel particles allows them to absorb a wide range of hazardous, genetic, and carcinogenic substances [24]. Diesel particle exposure can lead to coughs, itchy or burning eyes, and neuropsychiatric symptoms such as headache, vomiting, nausea, complicated breathing, chest tightness, and wheezing. [25]. On the other hand, biomass burning due to bushfire smoke and smoke from planned burns releases a large amount of PM that is very hazardous to human health [26]. These microscopic particles can spread throughout the distal lung areas, causing illnesses at chronic cardio-pulmonary. Long-term exposure to such fine particles has been associated with higher mortality risk. In addition, human lungs are severely harmed by cigarette smoke particles (CSP) [27]. Usage of Tobacco emits 5.2 million tonnes of methane and 2.6 million tonnes of CO_2 into the environment [28]. Around 7000 compounds have been found in cigarettes and other tobacco products, 250 of which are harmful to people and 70 of which are carcinogenic to humans [29]. This is because of inducing epithelial cell mutagenesis and so

biologically caused cancers. Smoking is still a significant cause of mortality and disability worldwide [30].

Coarse dust particles (>10 μm) usually lodge in the upper respiratory tract after being inhaled. Toxic dust particles pose a health risk regardless of where they lodge in the respiratory system. The dust particle (<10 μm) may stay suspended in the environment for weeks, and they can penetrate the deep lung airways [31]. The finer (⩽4 μm) dust particles are inhaled and eventually deposit in the pulmonary alveoli, causing chronic lung disease. Particles appear to be rapidly absorbed and deposited in the lung alveolar region [32]. The deposition of inhaled particles in human lungs is influenced by several parameters, including exposure concentration and particle parameters such as size, density, shape, and individual breathing conditions [33]. Particle deposition in the lungs is usually governed by inertial impaction, gravity sedimentation, and diffusion mechanism [34]. In addition, particle size grows, and hygroscopic growth influences particle deposition, causing particles to deposit in the respiratory tract [35].

Inhalation of aerosol particles is an efficient medicine delivery system in the treatment of lung illnesses [36, 37]. As a result, the dynamics of particle deposition in human lung airways are essential for human health to assess the efficacy of inhaled medicine therapy and the health implications of air pollution [38]. Therefore, many researchers have attempted to characterise particle deposition in the human lung, from total to local depositions [39, 40] and with findings ranging from empirical to numerical models [41-43]. Particles coming from various sources have a variety of sizes and chemical compositions [44]. Several studies on the impact of particle size on deposition have found that finer particles are more likely to be deposited in the deep lung airways [45, 46]. However, few studies have considered pollutant particles with different densities.

This study aims to quantify the deposition of particles with various densities and various sizes in human lungs under different breath conditions so that health risks related to particle exposure from various sources may be assessed. Airflow and particle deposition in a human lung are simulated numerically by CFD. We investigated the effects of both size and density of particles for calculating the deposition efficiency (DE) in a realistic human lung airway. Especially, we analyse three typical forms of pollutant particles: traffic, smoke, and dust, and analyse which particles are deposited in which part of lung airways. We also separated the contributions of inertial impaction and Brownian diffusion from each other to find out the fundamental mechanisms of particle deposition. The outcomes of this study will provide quantitative knowledge of how pollutant particle TD in the human lung airways is affected by particle size, density, and physical activity.

Nomenclatures			
p	Fluid pressure	ρ	Air density
T	Fluid temperature	ρ_p	Particle density
D	Hydraulic diameter	μ	Molecular viscosity
S_t	Stokes number	Δt	Particle time step
Q_{in}	Flow rate	G_i	Gaussian random number
u_i^p	Particle velocity	S_0	Spectral intensity function
d_p	Particle diameter	ν	kinematic viscosity
u_i	Fluid velocity	K_B	Boltzmann constant
Re_P	Particle Reynolds number	C_c	Stokes-Cunningham
F_{Di}	Drag force	λ	Gas molecules' mean free path
F_{gi}	Gravitational force	d_{ij}	Deformation tensor
F_{Bi}	Brownian force	η_d	Deposition efficiency
F_{Li}	Saffman's lift force	U_τ	Friction velocity
C_D	Drag coefficient	τ_w	Wall shear stress
u_0	Fluid inlet velocity	η_e	Escaping rate

2. **Numerical method**

The breathing pattern, particle shape, and particle size are the key factors that influence particle deposition in human lung airways [47-49]. Diffusion and sedimentation are the primary deposition mechanisms for nanoscale particles during slow breathing (resting activity). When the particle size is in the nanoscale, the contribution of Saffman's lift force and Brownian diffusion has been observed to be significant [50, 51]. In the study by Rahman, Zhao, Islam, Dong and Saha [52], Saffman's lift force and Brownian diffusion's combined mechanism is defined as diffusion. At intense breathing (exercise mode), the inertial impaction mechanism for microscale particle deposition contributes to particle TD more than diffusion. As a result, several investigations on microparticle TD in human lungs focus only on impaction mechanisms [43, 53]. However, when the particle size is in between nano- and micro-scales, both impaction and diffusion should be considered if their contributions to particle TD do not differ from each other. In this study, a numerical model that considers all the particle TD mechanisms including diffusion, sedimentation, impaction and Saffman's lift forces are used to simulate TD of a variety of particles.

2.1. Reconstructed anatomical model

The three-dimensional (3D) anatomical model, including the mouth-throat area and the tracheobronchial upper lung airways shown in Figure 1, was generated using digitised CT scans of a 50-year-old person. For the convenience of discussion of Particle TD in different areas, the lung model is divided into Parts A-I as seen in Figure 1.

2.2. Airflow model

ANSYS FLUENT (version 19.2) software is used to solve the airflow and particle TD in the lung airways. The governing equations for simulating the flow are the Reynolds-averaged Navier-Stokes (RANS) equations:

$$\frac{\partial \rho}{\partial t} + \frac{\partial}{\partial x_i}(\rho u_i) = 0 \quad (1)$$

$$\frac{\partial}{\partial t}(\rho u_i) + \frac{\partial}{\partial x_j}(\rho u_i u_j) = -\frac{\partial p}{\partial x_i} + \frac{\partial}{\partial x_j}\left[\mu\left(\frac{\partial u_i}{\partial x_j} + \frac{\partial u_j}{\partial x_i}\right)\right] + \frac{\partial}{\partial x_j}(-\rho\overline{u_i' u_j'}) \quad (2)$$

where t is time, x_i (i=1,2 and 3) are the Cartesian coordinates, u_i is the fluid velocity in the x_i-direction, p is the fluid pressure, ρ is the air density, μ is the molecular viscosity. The Reynolds stresses of turbulence are represented by $\rho\overline{u_i' u_j'}$ on the right-hand side of equation (2).

In this study, the realisable k-ε turbulence model is used for simulating the governing equations. It performs better than the standard k-ε turbulence model in a variety of complex flow conditions, including rotating homogeneous shear flows, boundary-free shear flows, channel and flat boundary layer flow with and without pressure gradients, and backwards-facing step flow [54]. It has been demonstrated that the realisable k-ε model can accurately predict the flow of complicated lung geometries without the requirement for near-wall adjustment [55-57].

The RANS equations are solved using the second-order upwind and pressure-velocity coupling schemes in FLUENT. The inlet of the lung model has a uniformly distributed velocity, and all its exits have zero gauged pressure. The boundary conditions at the outlets strongly influence the airflow partitions. As a result, Luo and Liu [58] have tested zero pressure at the outlet and outflow boundary conditions (i.e., a zero normal gradient for all flow variables except pressure). As a result, they observed that the airflow rate is identical to each outlet given the outflow boundary condition. Therefore, they conclude that zero pressure's outlet boundary condition is more acceptable than the outflow boundary condition. The airway wall was considered stationary and smooth with a non-slip boundary condition [51, 59, 60].

2.3. Particle transport model

The current particle TD model is a one-way coupling model that considers particle movement due to airflow but ignores particle effects on airflow [61, 62]. When the particle volume concentration is larger than 15%, two-way models that account for particle–particle interaction are needed. However, in all drug delivery applications, the volume concentration is less than 15% [63]. Therefore, collision-free conditions can be used to simulate the transport of dilute, suspended particles in the human lung,

or particle-particle interaction can be eliminated [64]. Because direct particle-particle interactions may be neglected if the particle suspension entering the tracheobronchial airway is dilute [63, 65]. As a result, most of the published studies did not include particle-particle interactions [66]. Particle TD in lung airways is modelled using the Lagrangian approach. The equation of motion of each individual particle is expressed as [51, 61]:

$$\frac{d\boldsymbol{u}_i^p}{dt} = \boldsymbol{F}_{Di} + \boldsymbol{F}_{gi} + \boldsymbol{F}_{Bi} + \boldsymbol{F}_{Li} \tag{3}$$

where u_i^p is particle velocity in the x_i-direction, $\boldsymbol{F}_{Di}$, $\boldsymbol{F}_{gi}$, $\boldsymbol{F}_{Bi}$ and $\boldsymbol{F}_{Li}$ are, respectively, the drag force, gravitational force, Brownian force, and Saffman's lift force per unit mass. The following formula determines the gravitational force:

$$\boldsymbol{F}_{gi} = \left(\frac{\rho_p - \rho}{\rho}\right)\boldsymbol{g} \tag{4}$$

where $\boldsymbol{g}$ denotes gravitational acceleration and $\rho_p$denotes particle density. The drag force is calculated using the following formula:

$$\boldsymbol{F}_{Di} = \frac{18\mu}{\rho_p d_p^2} C_D \frac{Re_p}{24}(\boldsymbol{u}_i - \boldsymbol{u}_i^p) \tag{5}$$

where $Re_p = \rho d_p \left|\boldsymbol{u}_i^p - \boldsymbol{u}_i\right|/\mu$ and the drag coefficient C_D for the spherical particles is calculated by [67]:

$C_D = a_1 + \frac{a_2}{Re_p} + \frac{a_3}{Re_p^2}$ for $0 < Re_p < 10$.

where a_1, a_2, a_3 are functions of the Reynolds number Re_P given by:

$$a_1, a_2, a_3 = \begin{cases} 0, & 24, & 0 & 0 < Re_p < 0.1 \\ 3.690, & 22.73, & 0.0903 & 0.1 < Re_p < 1 \\ 1.222, & 29.17, & 3.89 & 1 < Re_p < 10 \\ 0.617, & 46.50, & -116.67 & 10 < Re_p < 100 \\ 0.364, & 98.33, & -2778 & 100 < Re_p < 1000 \\ 0.357, & 148.62, & -47500 & 1000 < Re_p < 5000 \\ 0.46, & -490.546, & 578700 & 5000 < Re_p < 10000 \\ 0.519, & -1662.5, & 5416700 & Re_p > 10000 \end{cases}$$

Brownian motion describes the random, uncontrollable movement of particles in a fluid when molecules interact with each other [68]. It is strong in a less viscous fluid at a higher temperature with smaller particles [69]. Brownian motion in the air is unnoticeable if the particle size is bigger than 1 μm [70]. Brownian force that causes Brownian motion is defined as:

$$\boldsymbol{F}_{Bi} = \boldsymbol{G}_i \sqrt{\frac{\pi S_0}{\Delta t}} \tag{6}$$

where G_i is a Gaussian random number with unit variance and zero mean, Δt is the particle time step, and S_0 is the spectral intensity function associated with the diffusion coefficient by:

$$S_0 = \frac{216\nu k_B T}{\pi^2 \rho_p d_p^2 \left(\frac{\rho_p}{\rho}\right)^2 C_c} \tag{7}$$

where, ν is the kinematic viscosity, $K_B = 1.380649 \times 10^{-23}$ J/K is the Boltzmann constant, $T = 300K$ is the absolute fluid temperature, and C_c is the Stokes-Cunningham slip correction coefficient as

$$C_c = 1 + \frac{2\lambda}{d_p}\left(1.257 + 0.4e^{-\left(\frac{1.1 d_p}{2\lambda}\right)}\right) \tag{8}$$

where, the gas molecules' mean free path (λ) is 65 nm [71]. The lift force of Saffman is calculated using the following formula:

$$\boldsymbol{F}_{Li} = \frac{2K\nu^{\frac{1}{2}}\rho d_{ij}}{\rho_p d_p (d_{lk} d_{kl})^{\frac{1}{4}}}(\boldsymbol{u}_j - \boldsymbol{u}_j^p) \tag{9}$$

where, $K = 2.594$ is the constant coefficient of Saffman's lift force and $d_{ij} = (\partial u_i/\partial x_j - \partial u_j/\partial x_i)/2$ is the deformation tensor of the flow velocity.

In the simulations, 81000 spherical particles were released randomly at one time from the inlet boundary. A 'trap' condition is implemented on the airway walls for particle deposition, and an 'escape' condition is implemented at the outlets [72-74]. In the escape condition, the particles can pass through the output boundary without being reflected back. In the trap condition, particles colliding with the inner surface of the lung airways are trapped. This "trap" condition seems appropriate as the airway walls contain mucus which is very sticky [75, 76].

2.4. Particle deposition efficiency calculation

The percentages of particles absorbed (trapped) on the inner surfaces of the human lung airways are referred to as deposition efficiency (η_d) and it is calculated by:

$$\eta_d(\%) = \frac{\text{The number of particles deposited in a given area}}{\text{Total number of particles inhaled through the mouth}} \times 100$$

3. Grid dependency study and model validation

3.1 Grid dependency study

Figure 2 (a) to (c) show the computational mesh near the asymmetric mouth-throat area, bronchioles section, and part of the lung airways, respectively. Near the walls, ten-layer smooth inflation was used to guarantee that the boundary layer flow was accurately simulated (Figure 2c). At carinal angles, denser mesh is used for accurate resolution of complex flows.

The grid independence test is performed using six mesh sizes with cell numbers of 632006 (Mesh-1), 1300952 (Mesh-2), 2557333 (Mesh-3), 3053482 (Mesh-4), 3870593 (Mesh-5) and 4568314 (Mesh-6), respectively. The densest mesh has a grid size of 0.1 mm near the wall, and the mesh size is inversely proportional to the number of elements. The pressure and average velocity magnitude are shown in Figures 3 (b), (c), and (d) for the three sections indicated in Figure 3 (a), where *X* is the direction along the section diameter. Increasing the grid number does not influence pressure and velocity if the mesh density exceeds Mesh-4 as can be demonstrated. The maximum difference between the velocities from Mesh-5 and mesh-6 is about 0.01%. The velocity and pressure converge at Mesh-5 also. The non-dimensional wall unit (y^+) is defined inside the boundary layer as

$$y^+ = \frac{\rho U_\tau y}{\mu} \tag{10}$$

where $U_\tau \left(= \sqrt{\frac{\tau_w}{\rho}}\right)$ is the friction velocity, *y* (=0.143 mm for Mesh-5) is the distance between the first layer of mesh points and the boundary, and τ_w is the wall shear stress. The maximum y^+ of Mesh-5 in our simulation is 3.2. Pan, Lin, Wei and Chen [77] found RANS and LES solutions for structured and unstructured meshes agreed with experimental data when the y^+ value was 3.5.

Figure 4 shows the variation of the calculated deposition efficiency with a mesh element number. The deposition efficiency remains virtually unchanged after the mesh density is higher than Mesh-4 with 3.05 million elements. The Mesh-5 with 3.87 million elements was used in all the numerical simulations in this study.

3.2 Model validation

The validation of micro and nano-particles has already been conducted in our previous studies [52, 57]. To further validate the numerical method for nanoparticles, the present CFD results are compared to experimental data [78, 79] and numerical predictions [80, 81] of particle deposition in the mouth-throat area of a realistic lung. For a nanoparticle simulation, Figure 5 (a) shows the predicted deposition efficiency as a function of particle diameter for a constant of flow rate of 4 L/min. In addition, Figure 5(b) shows the particle deposition efficiency as a function of Stokes number defined as $\mathrm{S_t} = \rho_p d_p^2 u_0 / 18\mu \mathrm{D}$ for microparticles simulation, where u_0 denotes the inlet velocity at the boundary, and *D* (=0.0124 m) denotes the hydraulic diameter. In Figure 5 (a) the deposition efficiency of nanoparticles decreases with the increase of particle size. According to the linear relationship between particle size and Stokes number, it can be further deduced that the deposition efficiency of nanoparticles decreases with the increase of the Stokes number. However, the deposition efficiency of microparticles increases as the Stokes number increases. The relationship between deposition efficiency and Stokes number and

particle diameter is well predicted by numerical models in Figure 5. Figures 5 (a) and (b) show that the current model can accurately calculate particle TD of micro-and nanoparticles in a realistic 3D mouth-throat and tracheobronchial airway of a lung.

4. Results and discussion

The airflow dynamics and particle deposition are investigated in this study under three flow conditions: low-level breathing (Q_{in}=15 L/min) at rest, moderate activity breathing (Q_{in} =30 L/min) at the walk, and intense breathing (Q_{in} =60 L/min) during excise [82, 83].

4.1. Airflow Characteristics

Velocity profiles at various locations in the mouth-throat, trachea, and bronchioles regions are compared with each other to investigate airflow patterns in lung airways. The velocity profiles for the three flow rates along the diameter direction (*X*-direction) of four selected cross-sections (indicated in Figure 1) are shown in Figure 6. The velocity is nondimensionalised by the inlet velocity of the whole lung model u_0. Non-dimensional velocity distributions of different flow rates follow a similar trend, but they are not the same because of the difference in the Reynolds number. The velocity on each section is very asymmetric because of the complexity of the lung geometry. The mouth-throat area (*jj′*) had the maximum non-dimensional velocity in all selected regions, whereas the bronchioles (*ll′*) had the lowest velocity. Velocities changed largely at the mouth-throat region with complex airway structure. The velocity is reduced at kk' because of the increase in the cross-sectional area. In addition to the effect of airway geometry complexity, the velocity distribution in each branch becomes very non-uniform once the air passes through a bifurcation. However, as illustrated in Figure 6 (d), the velocity profile (*mm′* section) is symmetrical parabolic in the lower airway. The difference velocity distributions of different flow rates are found to be the maximum at the lowest section mm'.

4.2 Wall Shear Stress

Figure 7 quantitatively depicts the averaged non-dimensional shear stress ($\tau/(\rho u_0^2)$) along the inner wall of the lung as a function of flow rate in the upper lung airway model on seven sections defined in Figure 1, where wall shear stress τ is defined as the tangential force per unit area exerted by the flowing fluid on the wall surface. The wall shear stress distributions in the seven sections for different flow rates follow a similar trend but not the same. The wall shear stress varies considerably with each section at the lung airway because of the flow rate variation caused by complicated lung geometry.

Figure 8 illustrate the pressure distribution along the lung airways at several positions, from the mouth to the bronchioles. As air enters the deep lung, the pressure drops because of the energy loss. The biggest drop happens when air flows through a long airway between sections 1 and 2. The cross-section areas of sections 1 and 2 are 0.00024 m^2 and 0.00021 m^2, respectively. Due to the higher cross-section area, the pressure in Section 1 is higher than in the remaining sections (sections 2–7). According to Bernoulli's principle, a decrease in velocity causes an increase in pressure even if no energy is lost. A significant pressure drop is observed at a low flow rate of 15 L/min. It was observed that the pressure decrease for a low flow rate of 15 L/min is 53% more than that for a high flow rate of 60 L/min. Because the volume flow rate decreases, the pressure drops dramatically from section 1 to section 7. As a result, the pressure in all sections decreases as the flow rate decreases. As a result, breathing air into a low-flow lung is more complex than breathing air into a high-flow lung.

4.3 Particle Deposition

We looked at three different forms of pollutant particles: traffic, smoke, and dust particles. Pollutant particles come from various sources, depending on the environmental factors, ranging in size and chemical composition, such as nitrogen oxides (NO and NO_2), carbon monoxide (CO), and sulphur dioxide (SO_2) [44, 84-86]. However, whereas particle size has generally been noted as a factor in the deposition in human lungs, the impact of particle chemical composition has been neglected in the current study. Therefore, the impact of particle chemical composition for the current study was demonstrated using the bulk density. Bulk density was used to express the difference in chemical composition between particles [87]. Therefore, we assumed that the density of traffic, smoke and dust particles are 2000 kg/m^3, 1120 kg/m^3 and 400 kg/m^3, respectively [88, 89]. The diameter of these pollutant particles in the range of 5nm $\leq d_p \leq$ 10 μm are examined.

To quantify the contributions of impaction ($\boldsymbol{F}_{\mathrm{Di}}$ and $\boldsymbol{F}_{\mathrm{gi}}$), Brownian diffusion ($\boldsymbol{F}_{Bi}$), and Saffman's lift force ($\boldsymbol{F}_{Li}$) using numerical simulations in two scenarios: (1) only the impaction term is included in the particle motion equation, and (2) all impaction, Brownian diffusion, and Saffman's terms are taken into consideration. Because both Brownian diffusion and Saffman's lift contribute to the motion of particles in crossflow directions, they are combined together and referred to as diffusion in this study [52]. As a result, situations (1) and (2) are referred to as impaction only and impaction+diffusion, respectively, in the discussion. The simulations of nano- to micron-scale particles in the range of 5 nm $\leq d_p \leq$ 10 μm and the particle densities of 2000 kg/m^3, 1120 kg/m^3 and 400 kg/m^3 are performed to determine the contribution of each mechanism at various particle

sizes and densities. In the discussion, the particles with densities of 2000 kg/m^3, 1120 kg/m^3 and 400 kg/m^3 are referred to as traffic, smoke and dust, respectively.

Figure 9 (a), (b) and (c) depict the variation of particle deposition efficiency in the whole lung model with particle diameter for three types of pollutants and three flow rates Q_{in}=15 L/min, 30 L/min, and 60 L/min. Simulations with impaction only (diffusion terms switched off in the equations) are also conducted, and the results with impaction only are denoted by $\eta_{d,I}$, as presented in Figure 10. Table 1 lists the particle deposition rates at the largest and smallest particle diameters d_p=10 μm, and 5 nm. It can be found that the same size particle, d_p=10 μm but different density pollutant particles have significant different deposition efficiencies. The largest flow rate Q_{in}=60 L/min and largest particle diameter d_p=10 μm have the maximum total particle deposition efficiencies for traffic, smoke, and dust particle in Figure 9 (a) and Table 1. The deposition rate at d_p=10 μm decreases with the decrease of flow rate.

The effects of the particle density and flow rate on the deposition of 5-nm particles are different from that of 10-μm particles in the following aspect. First, the density has a very weak effect on the deposition rate of 5-nm particles, while an increase of the density from 400 kg/m^3 to 2000 kg/m^3 causes a significant increase of the deposition rate of 10-μm particles, for example by around three times for all the flow rates. Second, the particle deposition rate of 5 nm particles increases but that of 10 μm decreases with the flow rate increase. The increase of the deposition rate with the increase in density of 10-μm particles affects the distribution particles in the present lung model. The smallest deposition rate of 10-μm dust indicates the largest amount of 10-μm dust goes into the deeper lung [89].

Nanoscale particles follow streamlines due to the strong drag force, making it difficult for them to reach the airway wall only from the impaction mechanism [52, 90]. However, the Brownian and Saffman lift forces on nanoparticles increase with the decrease of the particle size. These forces in the crossflow direction enable particles to move towards the airway wall. As a result, the deposition rate rises in the nanoscale as particle size decreases. However, the deposition rate of the smallest nanoparticles caused by the diffusion effect is much smaller than that of the largest microparticles by impaction in Figure 9. Figures 9 also shows that an decrease in the flow rate increases η_d of nanoparticles because smaller flow velocity gives particles more time to move in the crossflow direction towards the wall due to diffusion [91, 92]. It can be seen in Table 1 that the deposition efficiencies of 5-nm particles at Q_{in}=60 L/min is nearly half of that at Q_{in}=15 L/min. The deposition efficiencies of 5-nm to 500-nm particles are small because both diffusion and impaction mechanisms are weak.

The reason why the deposition rate of microparticles increases with increasing particle size or flow rate can be explained by the inertial effect. When flow goes through curved airways, flow velocity

follows the curved airway, but large particles tend to stay on their original tracks due to the initial mechanism and hit the airway wall. This type of deposition mechanism is known as impaction [39, 53, 63, 93].

To quantify the contribution of impaction and diffusion to the particle deposition rate, the ratio of the deposition efficiency calculated using only impaction in Eq. (3), which is defined as $\eta_{\mathrm{d,I}}$ to the total diffusion efficiency $\eta_{\mathrm{d,}}$ when both impaction and diffusion are considered, for flow rates of 60 L/min, 30 L/min, and 15 L/min are presented in Figure 10 (a), (b) and (c), respectively.

The ratio $\eta_{\mathrm{d,I}}/\eta_{\mathrm{d}}$ of particles larger than 1000 nm is greater than 0.9 for all the three flow rates, suggesting a predominant contribution of impaction and negligible contribution from diffusion. In addition, the contribution of the impaction appears to be nearly independent on the particle size if the latter is greater than 1000 nm. The value of $\eta_{\mathrm{d,I}}/\eta_{\mathrm{d}}$ is found to be greater than 50% at the smallest particle size of 5 nm, indicating the effect of impaction is still comparable to the diffusion at this particle size. When the flow rate decreases from 60 L/min to 15 L/min, the impaction contribution of 5-nm particles is reduced from 88% to 57%.

The lung model is divided into parts A to I in Figure 1 and the distribution of the 10-μm particles among different parts is demonstrated by the bar charts in Figure 11. The type of the 10-μm particles significantly affects the deposition efficiency. At 60 L/min, the deposition efficiency in the mouth-throat part A is 98.7% for 10-μm heaviest traffic particles and it decreases to 22.0% for 10-μm lightest dust. For a specific particle type with d_{p}=10 μm, the highest flow rate of 60 L/min has the largest deposition efficiency because of its strongest impact mechanism. At the smallest flow rate of 15 L/min, 28.71% of traffic, 21.51% of smoke, and 14.73% of dust particles are deposited at region A. Because 10-μm traffic particles are mostly deposited (98.7%) at part A at 60 L/min, the deposition efficiencies at parts B to I are much smaller than those of smoke and dust as seen in Figure 11 (d). The deposition efficiency due to impaction increases with the increase of particle density. When the flow rate is reduced from 60L/min to 15 L/min, the number of 10-μm traffic particles passing through Part A increases, so the deposition efficiency of traffic particles is higher than those of smoke and dust particles as seen in Figure 11 (f). Impaction mechanism causes deposition where an airway bends, contracts, or bifurcates. Some deposition efficiencies are zero at part B in Figure 11 because part B is a vertical straight airway without bending or bifurcation.

Figure 12 shows the deposition efficiencies of 5-nm particles at parts A to I for three flow rates. The effect of the flow rate on the deposition efficiency of 5-nm particles is opposite to that of 10-μm particles. The deposition efficiencies of 5-nm particles at all the parts in Figure 12 increase as the flow rate decreases. However, the density of particles has a very small effect on the deposition efficiency

of 5-nm particles. Take the flow rate of 15 L/min in Figure 12 (c) as an example, the deposition efficiency in Part A only increases from 9.40% to 9.51% as the particle type changes from the heaviest traffic to the lightest dust. The effect of particle density on other parts and other flow rates are also similarly weak. At Part A, the deposition efficiency of 5-nm particles is significantly smaller than that of the deposition efficiency of 10-μm particles.

4.4 Visualisation of particle deposition

Figure 13 depicts the distribution of deposited particles in the human lung at a flow rate of 60 L/min. The deposition efficiencies of microparticles are much higher than those of nanoparticles but seemly more nanoparticles are deposited in the airways than microparticles in Figure 13. Under impaction mechanisms, particles are only deposited in the area where the airway bends, bifurcates or changes its diameter. A large number of 10-μm particles are found to be repeatedly deposited in the mouth-throat area where the airway is curved and rough and the bifurcation area. Repetitive deposition of many particles in the same areas makes the number of 10-μm particles look smaller than that of 5-nm particles in Figure 13 but not. Very small 10-μm particles are deposited in the long vertical straight airway (Part B) because impaction is weak in straight airways. About 98.72% of 10-μm traffic particles are deposited in the mouth-throat area (Part A), leaving nearly no particles passing this area. The reduced deposition efficiency of 10-μm dust particles in the mouth-throat area allows rest particles to either be deposited in the bifurcation areas or escape and enter the deep lung.

The deposited 5-nm particles are found to be much more evenly distributed in all the airways than 10-μm particles as shown in Figures 13 (d) -(f). Under the diffusion mechanism, the particles move in the crossflow direction, regardless of the shape of the airway. Even along the straight vertical airway (Part B), particles can also move in the crossflow direction through diffusion and reach the inner airway wall. The diffusion is strong only when the particle size is in the nanoscale. However, the diffusion does not make 10-μm particles move in the crossflow direction because it is negligibly weaker than the impaction mechanism.

4.5 Particle escaping rate

The escaping rate (defined as η_e) is defined as the percentage of particles that escape from the model's outlet and enter the deep lung. The escaping rate from all the exits equals to $1-\eta_d$. To understand the distribution of the escaped particles among different exits, the escape rates from the four exit regions for Q_{in}=60 L/min are represented in Figure 14. Each region has two exits, as shown in Figure 1, except region G+I where there are three exits. The escaping rate of the traffic particle in the regions E, F, H and I+G is nearly zero because most of the 10-μm traffic particles are deposited in

the upper part at 60 L/min. The escape rate of 10-μm particles increases as the particles changes from traffic to dust. The escaping rate of 10-μm dust particles that escape from the right side (regions E & F) and left side (regions H and I+G) are 28.76% and 37.79%, respectively. Therefore, more dust particles escape from the four exit regions compared to smoke and traffic particles.

The escaping rate of Region H is smaller than other regions because of the complex lung structure. The small dust particle can follow the fluid streamline and pass through the exit quickly because of the low inertial impaction effect. As a result, low-density dust particles sharply escape than high-density particles (Figure 14c) because the small exit in the lung model is present before H-region.

The significant effects of the density on the escaping rates of the three pollutant particles can be seen in Figure 14. The escaping rate of impaction only mechanism is a little bit higher than the rate of diffusion+ impaction mechanism because of the diffusion effect weakness. In every region (E, F, H, I+G-region), the influence of a high flow rate on the escape rate is greater than that of a micron-sized particle at the nanoscale ($d_p \leq 1000$ nm). As a result, particle size must be reduced to enhance the number of escaping particles that reach the deep lung.

5. Conclusions

Numerical simulations were used to analyse TD of nano- and micro-sized pollutant particles in the mouth-throat and tracheobronchial lung airways of a human lung. The effects of particle density, particle size and flow rate on deposition efficiency were investigated. The simulations include three particle densities, three flow rates and five particle sizes in micro and nanoscales. The contributions of the impaction and diffusion mechanisms were evaluated. The key findings of the numerical study are listed below;

- The strong impaction mechanism makes most of the 10-μm particles deposited in the human lung airway model, leaving an extremely small number of particles entering the deep lung. The contribution of impaction on the deposition efficiencies of 500-nm to 10-μm particles is over 97.6% when the flow rate is between 15 L/min to 60 L/min. The contribution of impaction on the deposition of the smallest 5-nm particles and the lowest flow rate of 15 L/min is reduced to about 57.4%.
- The deposition efficiencies of nanoparticles with d_p=5 nm on all the parts of the lung model is only affected by the flow rate and is nearly independent of the particle density (Figure 12). However, the deposition efficiency of 10-μm particles in the human lung is significantly affected by particle density. It increases with the increase of particle density.

- The deposited nanoparticles are found to be more evenly distributed in airways than the deposited microparticles (Figure 12). This is because the airway geometry affects the impaction mechanism, but the diffusion mechanism is not. As proved in Figure 13 (a) and (b), impaction induced deposition only happens wherever the airway bends, bifurcates or change diameter, while diffusion occurs everywhere if it is strong.
- The analysis of the escaping rates shows that more particles enter the left side than the right side of the lung, regardless of particle size, particle density or flow rate. This uneven distribution of escaping rate is mainly due to the asymmetry of the geometry of the lung.
- It can be concluded that particles with large diameter, large density and large flow rate deposit at the upper lung, while particles with small diameter, small density and small flow rate enter the deep lung. If the particle diameter is extremely small (i.e. 5 nm), the density does not have a sensible influence on the particle deposition.
- It was found that not only small particles enter into the deep lungs, large (10 μm) dust particles with low density (400 kg/m^3) can also be able enter the deep airways. It is estimated that 64.28% of the particles can go into the deep lung.

Pollutant particles and their possible health consequences are a major concern because they cause pulmonary diseases. Through this study, it was found that different mechanisms make different particles deposited in different area of human lungs. This conclusion help design strategies of protecting human lungs from different kinds of pollutant. If particles are electrically charged, a improved model need to be developed in the future to consider the interparticle interaction, which enhances with the increase of electrical charge.

Conflicts of Interest

The authors state no conflict of interest.

Acknowledgments:

Mr Rahman acknowledges the support of the Australian Government Research Training Program's International Postgraduate Research Scholarship (IPRS). The authors also acknowledge that the WSU High-Performance VM machine provided the computational facilities.

REFERENCES

[1] K.-H. Kim, E. Kabir, S. Kabir, A review on the human health impact of airborne particulate matter, Environment international, 74 (2015) 136-143.

[2] Z. Pražnikar, J. Pražnikar, The effects of particulate matter air pollution on respiratory health and on the cardiovascular system, Slovenian Journal of Public Health, 51 (2012) 190-199.
[3] A.K. Patra, S. Gautam, P. Kumar, Emissions and human health impact of particulate matter from surface mining operation—A review, Environmental Technology & Innovation, 5 (2016) 233-249.
[4] J.O. Anderson, J.G. Thundiyil, A. Stolbach, Clearing the air: a review of the effects of particulate matter air pollution on human health, Journal of medical toxicology, 8 (2012) 166-175.
[5] N. Tahery, K. Zarea, M. Cheraghi, N. Hatamzadeh, M. Farhadi, S. Dobaradarn, M.J. Mohammadi, Chronic Obstructive Pulmonary Disease (COPD) and Air Pollution: A Review, Jundishapur Journal of Chronic Disease Care, 10 (2021).
[6] J.M. Borghardt, C. Kloft, A. Sharma, Inhaled therapy in respiratory disease: the complex interplay of pulmonary kinetic processes, Canadian respiratory journal, 2018 (2018).
[7] G. Collaborators, J. Ärnlöv, Global burden of 87 risk factors in 204 countries and territories, 1990–2019: a systematic analysis for the Global Burden of Disease Study 2019, The Lancet, 396 (2020) 1223-1249.
[8] T. Olaniyan, M. Dalvie, M. Jeebhay, Ambient air pollution and childhood asthma: a review of South African epidemiological studies: allergies in the workplace, Current Allergy & Clinical Immunology, 28 (2015) 122-127.
[9] A.J. Cohen, M. Brauer, R. Burnett, H.R. Anderson, J. Frostad, K. Estep, K. Balakrishnan, B. Brunekreef, L. Dandona, R. Dandona, Estimates and 25-year trends of the global burden of disease attributable to ambient air pollution: an analysis of data from the Global Burden of Diseases Study 2015, The Lancet, 389 (2017) 1907-1918.
[10] I. Manisalidis, E. Stavropoulou, A. Stavropoulos, E. Bezirtzoglou, Environmental and health impacts of air pollution: a review, Frontiers in public health, 8 (2020) 14.
[11] D.E. Schraufnagel, The health effects of ultrafine particles, Experimental & molecular medicine, 52 (2020) 311-317.
[12] M.A. Albrecht, C.W. Evans, C.L. Raston, Green chemistry and the health implications of nanoparticles, Green chemistry, 8 (2006) 417-432.
[13] K. Donaldson, X. Li, W. MacNee, Ultrafine (nanometre) particle mediated lung injury, Journal of aerosol science, 29 (1998) 553-560.
[14] R. Gao, N. Sang, Quasi-ultrafine particles promote cell metastasis via HMGB1-mediated cancer cell adhesion, Environmental Pollution, 256 (2020) 113390.
[15] G. Oberdörster, Pulmonary effects of inhaled ultrafine particles, International archives of occupational and environmental health, 74 (2000) 1-8.
[16] R.D. Peng, H.H. Chang, M.L. Bell, A. McDermott, S.L. Zeger, J.M. Samet, F. Dominici, Coarse particulate matter air pollution and hospital admissions for cardiovascular and respiratory diseases among Medicare patients, Jama, 299 (2008) 2172-2179.
[17] M. Diao, T. Holloway, S. Choi, S.M. O'Neill, M.Z. Al-Hamdan, A. Van Donkelaar, R.V. Martin, X. Jin, A.M. Fiore, D.K. Henze, Methods, availability, and applications of PM2. 5 exposure estimates derived from ground measurements, satellite, and atmospheric models, Journal of the Air & Waste Management Association, 69 (2019) 1391-1414.
[18] N. Englert, Fine particles and human health—a review of epidemiological studies, Toxicology letters, 149 (2004) 235-242.
[19] K. Donaldson, V. Stone, A. Seaton, W. MacNee, Ambient particle inhalation and the cardiovascular system: potential mechanisms, Environmental health perspectives, 109 (2001) 523-527.
[20] B. Brunekreef, B. Forsberg, Epidemiological evidence of effects of coarse airborne particles on health, European respiratory journal, 26 (2005) 309-318.
[21] A. Charron, R.M. Harrison, Fine (PM2. 5) and coarse (PM2. 5-10) particulate matter on a heavily trafficked London highway: sources and processes, Environmental science & technology, 39 (2005) 7768-7776.

[22] D. Hammond, S. Jones, M. Lalor, In-vehicle measurement of ultrafine particles on compressed natural gas, conventional diesel, and oxidation-catalyst diesel heavy-duty transit buses, Environmental monitoring and assessment, 125 (2007) 239-246.
[23] E.R.-F. de Sarabia, L. Elvira-Segura, I. Gonzalez-Gomez, J. Rodrıguez-Maroto, R. Munoz-Bueno, J. Dorronsoro-Areal, Investigation of the influence of humidity on the ultrasonic agglomeration of submicron particles in diesel exhausts, Ultrasonics, 41 (2003) 277-281.
[24] J. Zhao, V. Castranova, Toxicology of nanomaterials used in nanomedicine, Journal of Toxicology and Environmental Health, Part B, 14 (2011) 593-632.
[25] G. Ritchie, K. Still, J. Rossi Iii, M. Bekkedal, A. Bobb, D. Arfsten, Biological and health effects of exposure to kerosene-based jet fuels and performance additives, Journal of Toxicology and Environmental Health, Part B, 6 (2003) 357-451.
[26] H.J. Johnston, W. Mueller, S. Steinle, S. Vardoulakis, K. Tantrakarnapa, M. Loh, J.W. Cherrie, How harmful is particulate matter emitted from biomass burning? A Thailand perspective, Current Pollution Reports, 5 (2019) 353-377.
[27] K. Ravindra, A.K. Mittal, R. Van Grieken, Health risk assessment of urban suspended particulate matter with special reference to polycyclic aromatic hydrocarbons: a review, Reviews on environmental health, (2001).
[28] A.H. Buchanan, B.G. Honey, Energy and carbon dioxide implications of building construction, Energy and Buildings, 20 (1994) 205-217.
[29] M.B. Drummond, D. Upson, Electronic cigarettes. Potential harms and benefits, Annals of the American Thoracic Society, 11 (2014) 236-242.
[30] L. Ferrucci, G. Izmirlian, S. Leveille, C.L. Phillips, M.-C. Corti, D.B. Brock, J.M. Guralnik, Smoking, physical activity, and active life expectancy, American journal of epidemiology, 149 (1999) 645-653.
[31] E. Derbyshire, Natural minerogenic dust and human health, AMBIO: A Journal of the Human Environment, 36 (2007) 73-77.
[32] S. Bakand, A. Hayes, F. Dechsakulthorn, Nanoparticles: a review of particle toxicology following inhalation exposure, Inhalation toxicology, 24 (2012) 125-135.
[33] B.O. Stuart, Deposition and clearance of inhaled particles, Environmental health perspectives, 55 (1984) 369-390.
[34] J.-I. Choi, C.S. Kim, Mathematical analysis of particle deposition in human lungs: an improved single path transport model, Inhalation toxicology, 19 (2007) 925-939.
[35] B. Asgharian, A model of deposition of hygroscopic particles in the human lung, Aerosol science and technology, 38 (2004) 938-947.
[36] S. Azarmi, W.H. Roa, R. Löbenberg, Targeted delivery of nanoparticles for the treatment of lung diseases, Advanced drug delivery reviews, 60 (2008) 863-875.
[37] M. Nassimi, C. Schleh, H.D. Lauenstein, R. Hussein, H.-G. Hoymann, W. Koch, G. Pohlmann, N. Krug, K. Sewald, S. Rittinghausen, A toxicological evaluation of inhaled solid lipid nanoparticles used as a potential drug delivery system for the lung, European Journal of Pharmaceutics and Biopharmaceutics, 75 (2010) 107-116.
[38] Q. Deng, C. Ou, J. Chen, Y. Xiang, Particle deposition in tracheobronchial airways of an infant, child and adult, Science of the Total Environment, 612 (2018) 339-346.
[39] X. Chen, W. Zhong, X. Zhou, B. Jin, B. Sun, CFD–DEM simulation of particle transport and deposition in pulmonary airway, Powder technology, 228 (2012) 309-318.
[40] I. Balásházy, W. Hofmann, T. Heistracher, Local particle deposition patterns may play a key role in the development of lung cancer, Journal of Applied Physiology, 94 (2003) 1719-1725.
[41] W. Hofmann, Modelling inhaled particle deposition in the human lung—A review, Journal of Aerosol Science, 42 (2011) 693-724.

[42] V.K.H. Bui, J.-Y. Moon, M. Chae, D. Park, Y.-C. Lee, Prediction of aerosol deposition in the human respiratory tract via computational models: A review with recent updates, Atmosphere, 11 (2020) 137.
[43] X. Chen, Y. Feng, W. Zhong, B. Sun, F. Tao, Numerical investigation of particle deposition in a triple bifurcation airway due to gravitational sedimentation and inertial impaction, Powder Technology, 323 (2018) 284-293.
[44] C. Leoni, P. Pokorná, J. Hovorka, M. Masiol, J. Topinka, Y. Zhao, K. Křůmal, S. Cliff, P. Mikuška, P.K. Hopke, Source apportionment of aerosol particles at a European air pollution hot spot using particle number size distributions and chemical composition, Environmental Pollution, 234 (2018) 145-154.
[45] B. Asgharian, O.T. Price, Deposition of ultrafine (nano) particles in the human lung, Inhalation toxicology, 19 (2007) 1045-1054.
[46] W. Moller, K. Felten, K. Sommerer, G. Scheuch, G. Meyer, P. Meyer, K. Haussinger, W.G. Kreyling, Deposition, retention, and translocation of ultrafine particles from the central airways and lung periphery, American journal of respiratory and critical care medicine, 177 (2008) 426-432.
[47] C. Ou, H. Jian, Q. Deng, Particle Deposition in Human Lung Airways: Effects of Airflow, Particle Size, and Mechanisms, Aerosol and Air Quality Research, 20 (2020).
[48] C. Xu, X. Zheng, S. Shen, A numerical study of the effect of breathing mode and exposure conditions on the particle inhalation and deposition, Inhalation Toxicology, 32 (2020) 456-467.
[49] M. Yousefi, O. Pourmehran, M. Gorji-Bandpy, K. Inthavong, L. Yeo, J. Tu, CFD simulation of aerosol delivery to a human lung via surface acoustic wave nebulization, Biomechanics and modeling in mechanobiology, 16 (2017) 2035-2050.
[50] N. Dang Khoa, N.L. Phuong, K. Ito, Numerical modeling of nanoparticle deposition in realistic monkey airway and human airway models: a comparative study, Inhalation Toxicology, 32 (2020) 311-325.
[51] M.M. Rahman, M. Zhao, M.S. Islam, K. Dong, S.C. Saha, Aerosol Particle Transport and Deposition in Upper and Lower Airways of Infant, Child and Adult Human Lungs, Atmosphere, 12 (2021) 1402.
[52] M.M. Rahman, M. Zhao, M.S. Islam, K. Dong, S.C. Saha, Numerical study of nanoscale and microscale particle transport in realistic lung models with and without stenosis, International Journal of Multiphase Flow, 145 (2021) 103842.
[53] F. Huang, Y. Zhang, Z. Tong, X. Chen, R. Yang, A. Yu, Numerical investigation of deposition mechanism in three mouth–throat models, Powder Technology, 378 (2021) 724-735.
[54] T.H. Shih, W.W. Liou, A. Shabbir, Z. Yang, J. Zhu, A new k-ϵ eddy viscosity model for high reynolds number turbulent flows, Computers and Fluids, 24 (1995) 227-238.
[55] N.M. Isa, A.N.K. Ahmad Fara, N.Z. Asmuin, Investigation on the Turbulence Models Effect of a Coal Classifier by Using Computational Fluids Dynamics, Applied Mechanics and Materials, Trans Tech Publ, 2014, pp. 617-621.
[56] M. Abolhassantash, M. Tavakol, O. Abouali, M. Yaghoubi, G. Ahmadi, Deposition fraction of ellipsoidal fibers in the human nasal cavity-Influence of non-creeping formulation of hydrodynamic forces and torques, International Journal of Multiphase Flow, 126 (2020) 103238.
[57] M.M. Rahman, M. Zhao, M.S. Islam, K. Dong, S.C. Saha, Aging effects on airflow distribution and micron-particle transport and deposition in a human lung using CFD-DPM approach, Advanced Powder Technology, 32 (2021) 3506-3516.
[58] H. Luo, Y. Liu, Modeling the bifurcating flow in a CT-scanned human lung airway, Journal of Biomechanics, 41 (2008) 2681-2688.
[59] M.S. Islam, P. Larpruenrudee, S.C. Saha, O. Pourmehran, A.R. Paul, T. Gemci, R. Collins, G. Paul, Y. Gu, How severe acute respiratory syndrome coronavirus-2 aerosol propagates through the age-specific upper airways, Physics of Fluids, 33 (2021) 081911.

[60] P. Singh, V. Raghav, V. Padhmashali, G. Paul, M.S. Islam, S.C. Saha, Airflow and particle transport prediction through stenosis airways, International Journal of Environmental Research and Public Health, 17 (2020) 1119.
[61] K. Inthavong, K. Zhang, J. Tu, Numerical modelling of nanoparticle deposition in the nasal cavity and the tracheobronchial airway, Computer Methods in Biomechanics and Biomedical Engineering, 14 (2011) 633-643.
[62] A. Lintermann, W. Schröder, Simulation of aerosol particle deposition in the upper human tracheobronchial tract, European Journal of Mechanics-B/Fluids, 63 (2017) 73-89.
[63] M.S. Islam, S.C. Saha, E. Sauret, H. Ong, P. Young, Y. Gu, Euler–Lagrange approach to investigate respiratory anatomical shape effects on aerosol particle transport and deposition, Toxicology Research and Application, 3 (2019) 2397847319894675.
[64] Y. Tsuji, Multi-scale modeling of dense phase gas–particle flow, Chemical engineering science, 62 (2007) 3410-3418.
[65] W.-H. Chen, C.-M. Chang, J.K. Mutuku, S.S. Lam, W.-J. Lee, Analysis of microparticle deposition in the human lung by taguchi method and response surface methodology, Environmental Research, 197 (2021) 110975.
[66] Y. Feng, C. Kleinstreuer, Micron-particle transport, interactions and deposition in triple lung-airway bifurcations using a novel modeling approach, Journal of Aerosol Science, 71 (2014) 1-15.
[67] S. Morsi, A. Alexander, An investigation of particle trajectories in two-phase flow systems, Journal of Fluid mechanics, 55 (1972) 193-208.
[68] F. Torrens, G. Castellano, Brownian Motion, Random Trajectory, Diffusion, Fractals, Theory of Chaos, and Dialectics, Modern Physical Chemistry: Engineering Models, Materials, and Methods with Applications, Apple Academic Press2018, pp. 27-36.
[69] S.P. Jang, S.U. Choi, Role of Brownian motion in the enhanced thermal conductivity of nanofluids, Applied physics letters, 84 (2004) 4316-4318.
[70] T. Franosch, M. Grimm, M. Belushkin, F.M. Mor, G. Foffi, L. Forró, S. Jeney, Resonances arising from hydrodynamic memory in Brownian motion, Nature, 478 (2011) 85-88.
[71] J. Xi, A. Berlinski, Y. Zhou, B. Greenberg, X. Ou, Breathing resistance and ultrafine particle deposition in nasal–laryngeal airways of a newborn, an infant, a child, and an adult, Annals of biomedical engineering, 40 (2012) 2579-2595.
[72] M.S. Islam, P. Larpruenrudee, A.R. Paul, G. Paul, T. Gemci, Y. Gu, S.C. Saha, SARS CoV-2 aerosol: How far it can travel to the lower airways?, Physics of Fluids, 33 (2021) 061903.
[73] C. Wu, W. Yan, C. Rou, Y. Liu, G. Li, Numerical study on targeted delivery of magnetic drug particles in realistic human lung, Powder Technology, (2021).
[74] Q. Gu, S. Qi, Y. Yue, J. Shen, B. Zhang, W. Sun, W. Qian, M.S. Islam, S.C. Saha, J. Wu, Structural and functional alterations of the tracheobronchial tree after left upper pulmonary lobectomy for lung cancer, BioMedical Engineering OnLine, 18 (2019) 1-18.
[75] A. Ghosh, M.S. Islam, S.C. Saha, Targeted drug delivery of magnetic nano-particle in the specific lung region, Computation, 8 (2020) 10.
[76] M.S. Islam, S.C. Saha, T. Gemci, I.A. Yang, E. Sauret, Y. Gu, Polydisperse microparticle transport and deposition to the terminal bronchioles in a heterogeneous vasculature tree, Scientific reports, 8 (2018) 1-9.
[77] Y. Pan, C.-H. Lin, D. Wei, C. Chen, Experimental measurements and large eddy simulation of particle deposition distribution around a multi-slot diffuser, Building and Environment, 150 (2019) 156-163.
[78] Y.-S. Cheng, Y. Zhou, B.T. Chen, Particle deposition in a cast of human oral airways, Aerosol Science & Technology, 31 (1999) 286-300.
[79] Y.-S. Cheng, Y.-F. Su, H.-C. Yeh, D.L. Swift, Deposition of thoron progeny in human head airways, Aerosol Science and Technology, 18 (1993) 359-375.

[80] C. Kleinstreuer, Z. Zhang, Z. Li, W.L. Roberts, C. Rojas, A new methodology for targeting drug-aerosols in the human respiratory system, International Journal of Heat and Mass Transfer, 51 (2008) 5578-5589.
[81] J. Xi, P. Longest, Effects of oral airway geometry characteristics on the diffusional deposition of inhaled nanoparticles, Journal of biomechanical engineering, 130 (2008).
[82] M.S. Islam, P. Larpruenrudee, S.I. Hossain, M. Rahimi-Gorji, Y. Gu, S.C. Saha, G. Paul, Polydisperse Aerosol Transport and Deposition in Upper Airways of Age-Specific Lung, International Journal of Environmental Research and Public Health, 18 (2021) 6239.
[83] Q. Deng, C. Ou, Y.-M. Shen, Y. Xiang, Y. Miao, Y. Li, Health effects of physical activity as predicted by particle deposition in the human respiratory tract, Science of The Total Environment, 657 (2019) 819-826.
[84] C. Sophonsiri, E. Morgenroth, Chemical composition associated with different particle size fractions in municipal, industrial, and agricultural wastewaters, Chemosphere, 55 (2004) 691-703.
[85] G. D'amato, L. Cecchi, Effects of climate change on environmental factors in respiratory allergic diseases, Clinical & Experimental Allergy, 38 (2008) 1264-1274.
[86] G.-P. Bălă, R.-M. Râjnoveanu, E. Tudorache, R. Motișan, C. Oancea, Air pollution exposure—the (in) visible risk factor for respiratory diseases, Environmental Science and Pollution Research, 28 (2021) 19615-19628.
[87] Z. Zhang, H. Song, Z. Peng, Q. Luo, J. Ming, G. Zhao, Characterization of stipe and cap powders of mushroom (Lentinus edodes) prepared by different grinding methods, Journal of Food Engineering, 109 (2012) 406-413.
[88] A.R. Paul, F. Khan, A. Jain, S.C. Saha, Deposition of smoke particles in human airways with realistic waveform, Atmosphere, 12 (2021) 912.
[89] Q. Deng, L. Deng, Y. Miao, X. Guo, Y. Li, Particle deposition in the human lung: Health implications of particulate matter from different sources, Environmental research, 169 (2019) 237-245.
[90] Z. Zhang, C. Kleinstreuer, Airflow structures and nano-particle deposition in a human upper airway model, Journal of computational physics, 198 (2004) 178-210.
[91] C. Darquenne, Deposition mechanisms, Journal of aerosol medicine and pulmonary drug delivery, 33 (2020) 181-185.
[92] M.S. Islam, S.C. Saha, T. Gemci, I.A. Yang, E. Sauret, Z. Ristovski, Y. Gu, Euler-Lagrange prediction of diesel-exhaust polydisperse particle transport and deposition in lung: Anatomy and turbulence effects, Scientific reports, 9 (2019) 1-16.
[93] A. Farghadan, K. Poorbahrami, S. Jalal, J.M. Oakes, F. Coletti, A. Arzani, Particle transport and deposition correlation with near-wall flow characteristic under inspiratory airflow in lung airways, Computers in biology and medicine, 120 (2020) 103703.

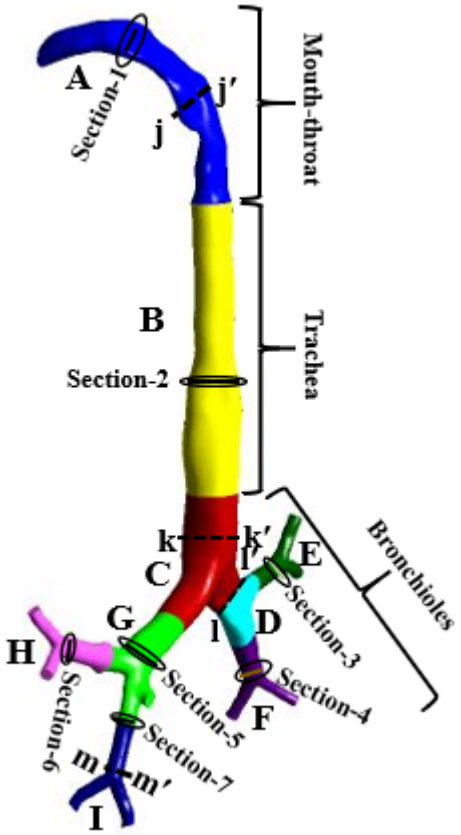

Figure 1: Reconstruction of realistic mouth–throat and tracheobronchial lung airways. The portions shown in the Figure will be referred to when the findings are presented.

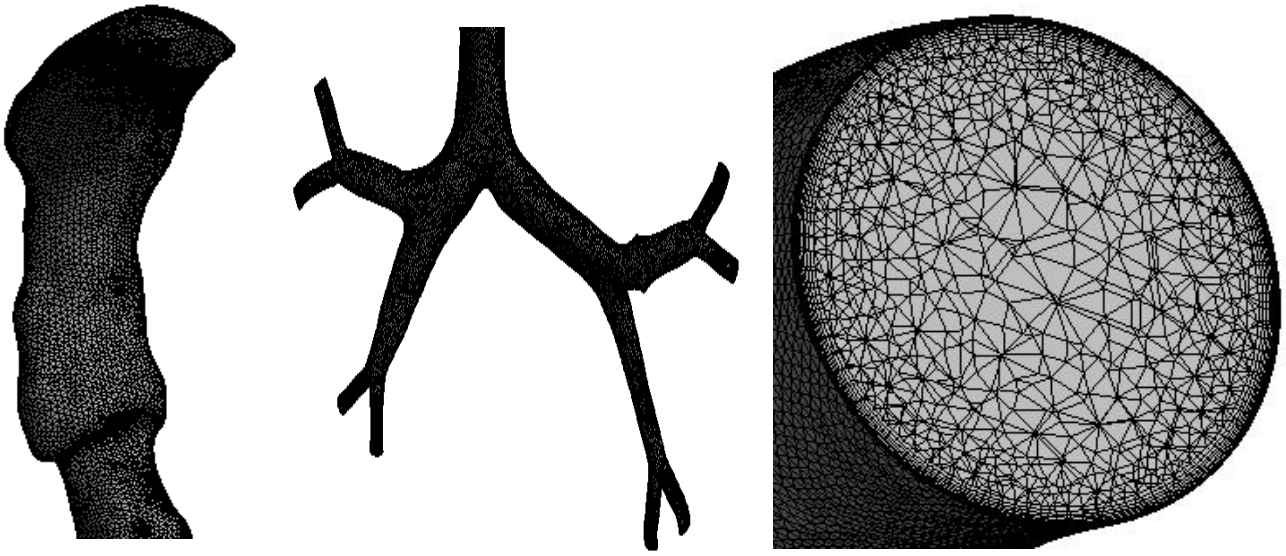

(a) (b) (c)

Figure 2. Mesh generation for (a) the mouth–throat portion, (b) the bronchioles portion, and (c) the inflation layer in an airway in a realistic lung model.

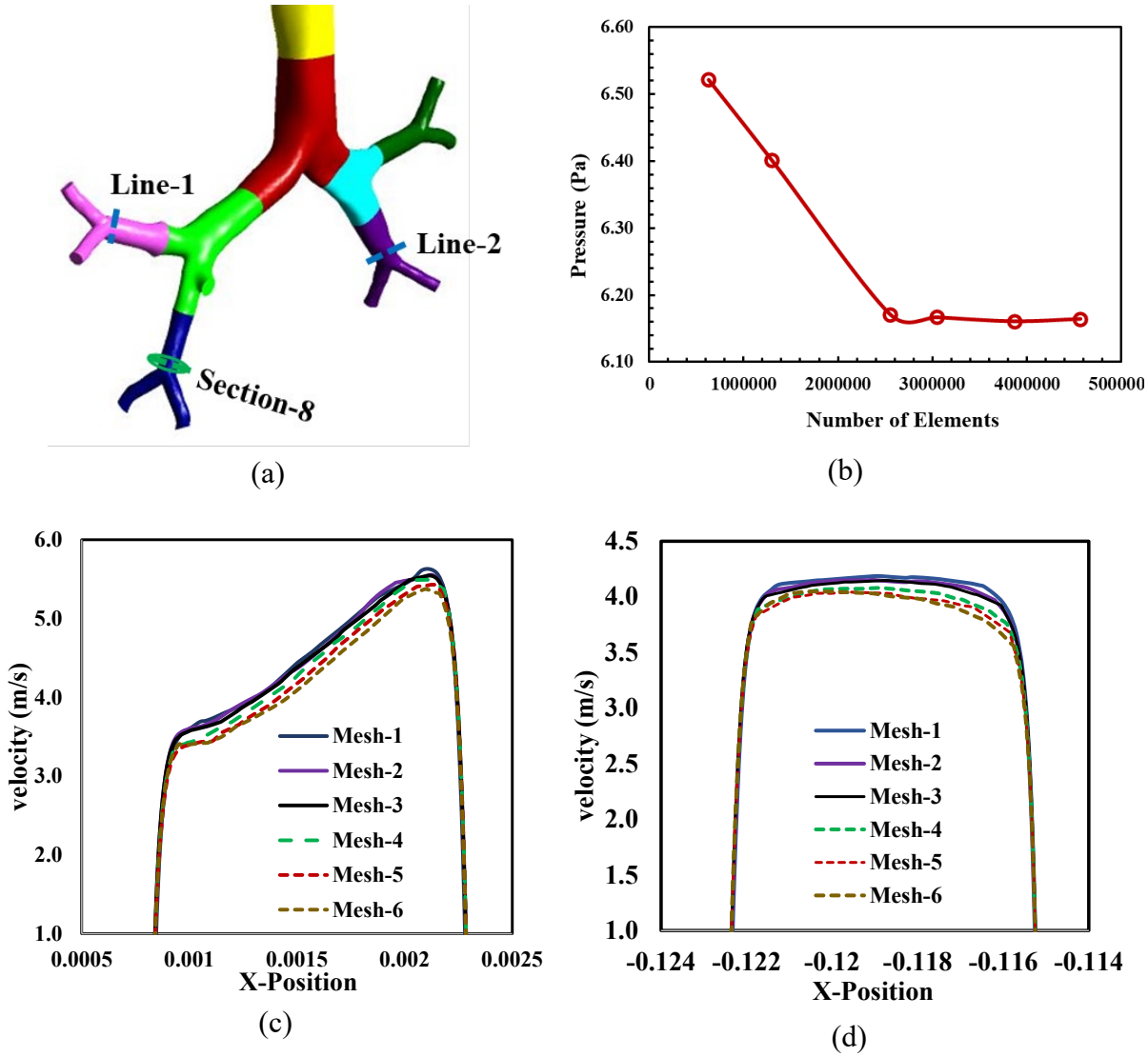

Figure 3. Grid refinement/mesh-independent test at the flow rate 60 L/min for realistic lung model, (b) average pressure as functions of grid number (average pressure calculated at the selected section-8 in Figure 3a); (c) velocity distribution at the Line-1; (d) velocity distribution at the Line-2 (average velocity calculated at the selected line in Figure 3a).

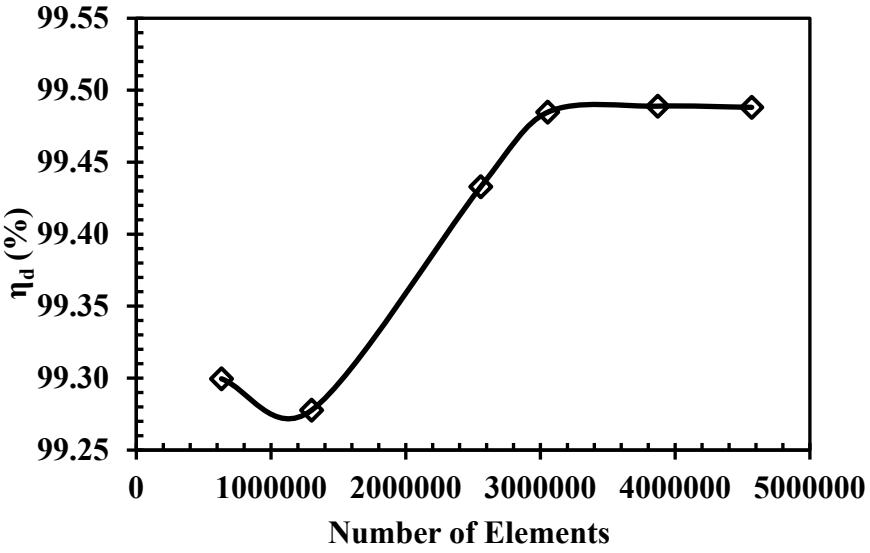

Figure 4. Deposition efficiency as a function of the grid number at the flow rate of 60 L/min. The diameter of traffic particles is 10 μm.

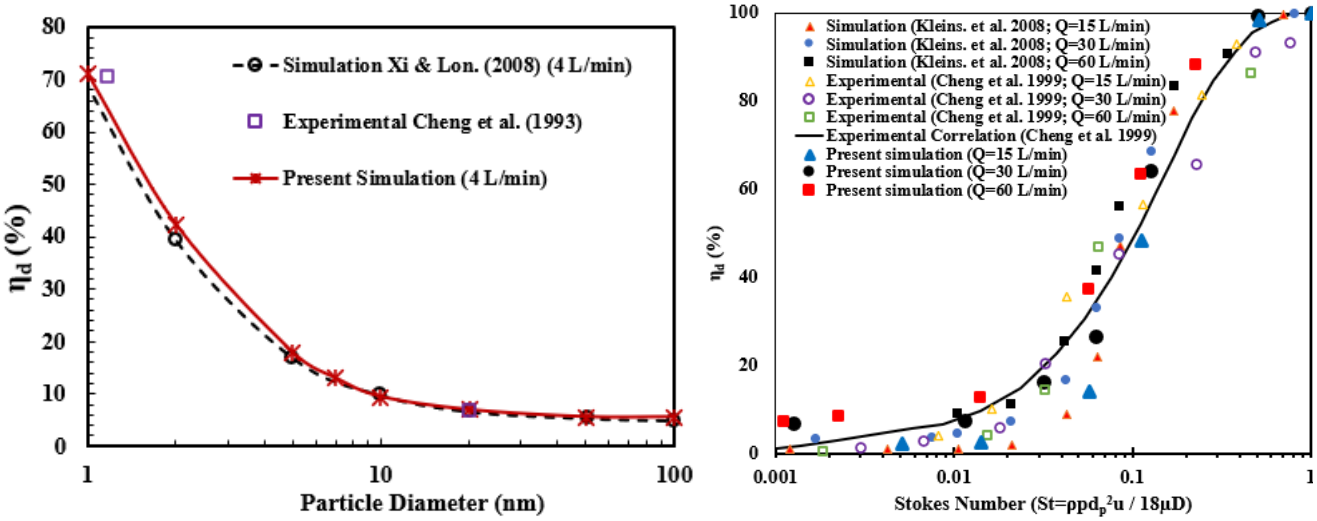

(a) Nanoparticles ($1\ \text{nm} \leq d_p \leq 100\ n\text{m}$) (b) Microparticles ($0.7\ \mu\text{m} \leq d_p \leq 42\ \mu\text{m}$)

Figure 5. Comparison of current nanoparticle and microparticle deposition simulations in the mouth-throat region with data from the literature (Cheng et al., 1999; Kleinstreuer et al., 2008; Xi and Longest, 2008).

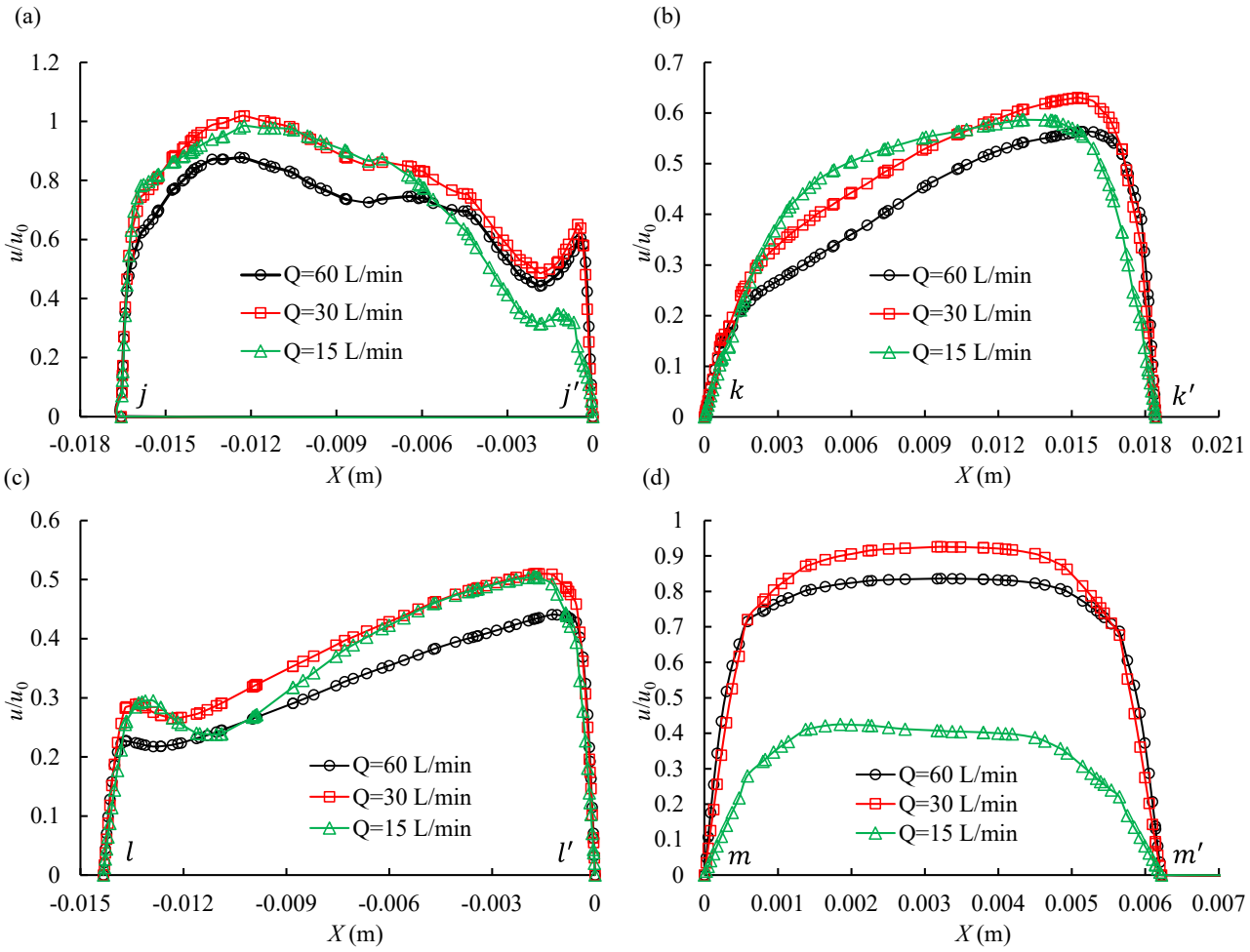

Figure 6. Velocity profiles under different flow rates, (a) Line jj′, (b) Line kk′, (c) Line ll′, and (d) Line mm′ (Figure 1 illustrates the lines).

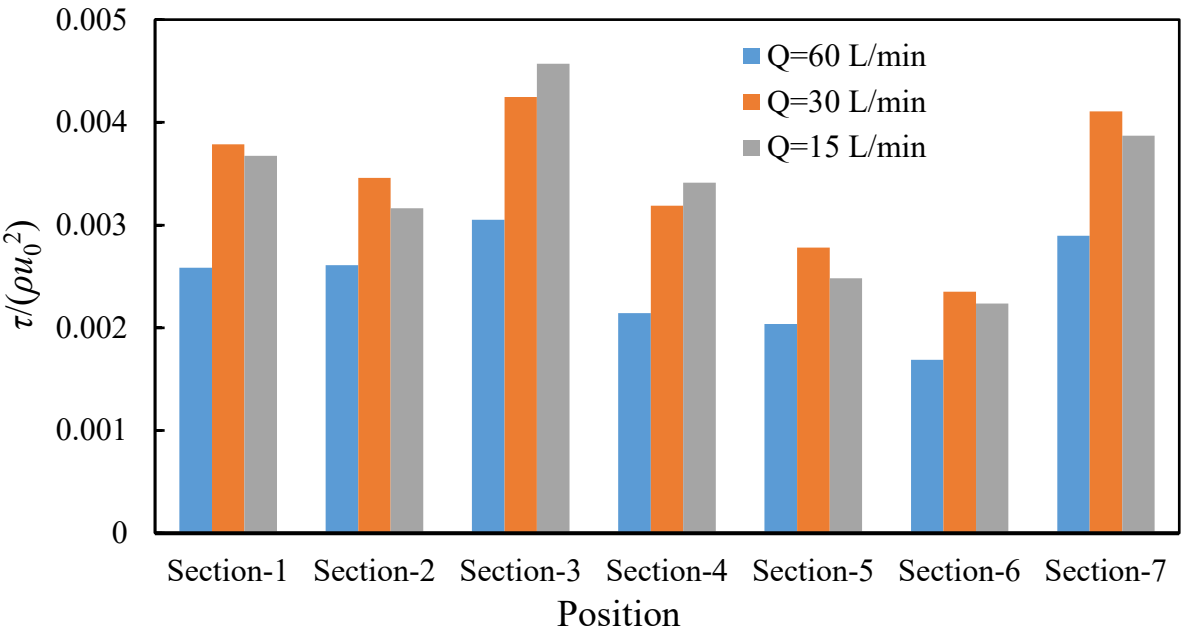

Figure 7. Averaged wall shear stress for a particular lung portion is indicated in Figure 1. The traffic particle diameter is 10-μm.

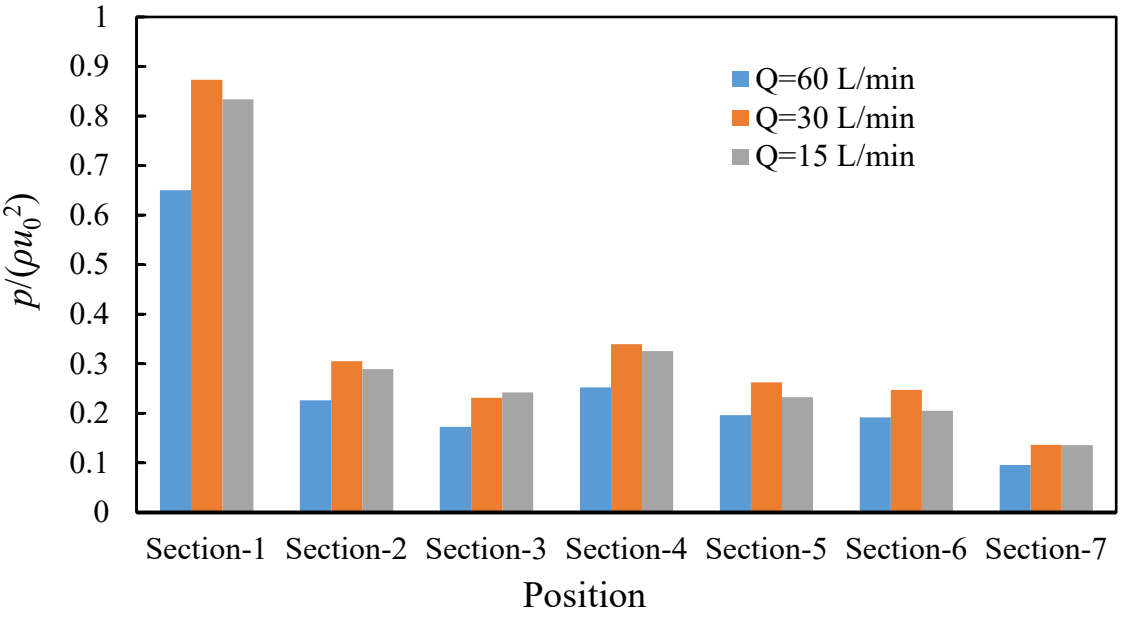

Figure 8. Pressure drop at three distinct flow rates in a different section of the realistic lung model, d_p=10 µm (traffic particle); the section numbers are shown in Figure 1.

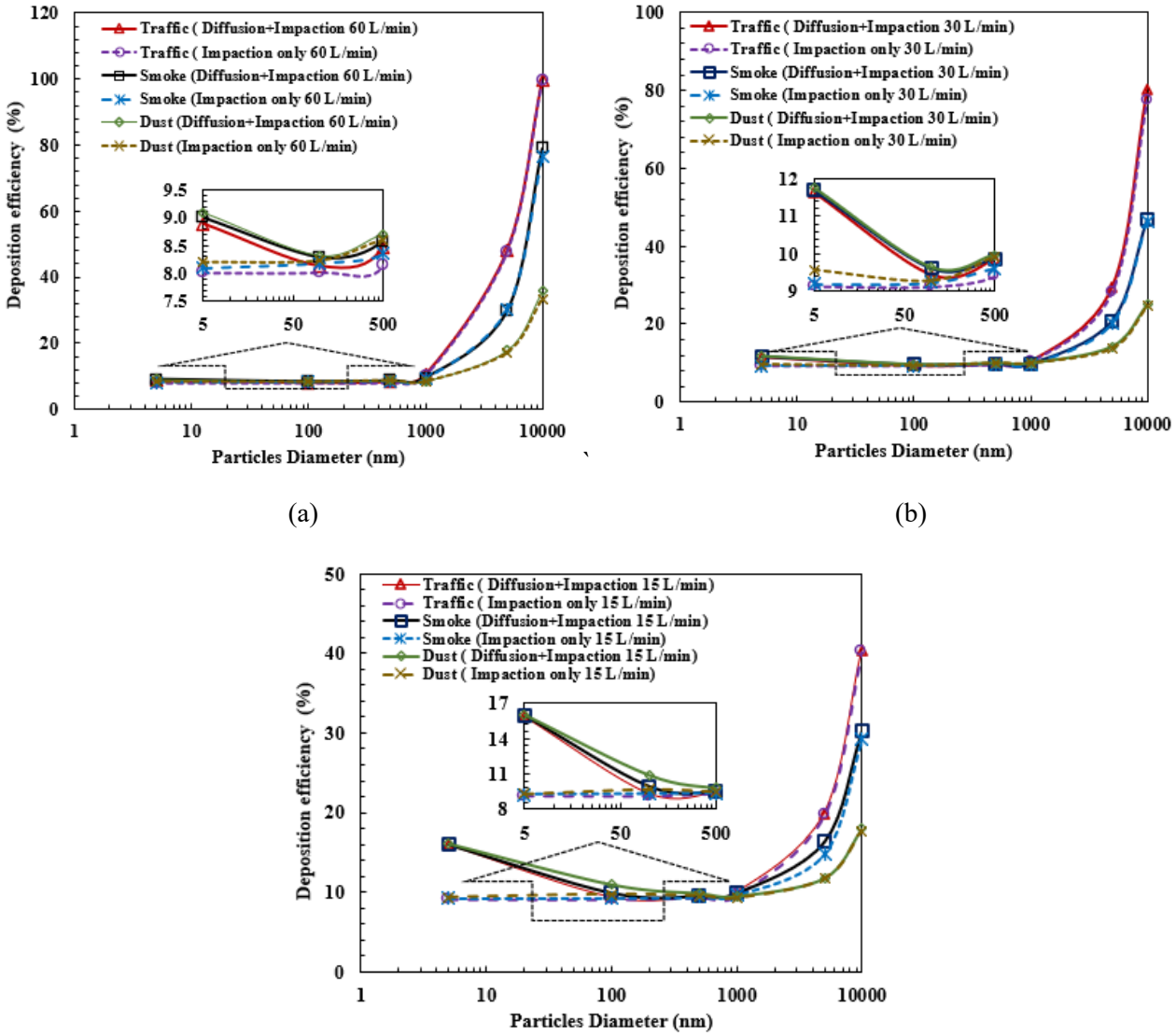

Figure 9. Particle deposition efficiency in the lung model for (a) Q_{in}=60 L/min; (b) Q_{in}=30 L/min and (c) Q_{in}=15 L/min.

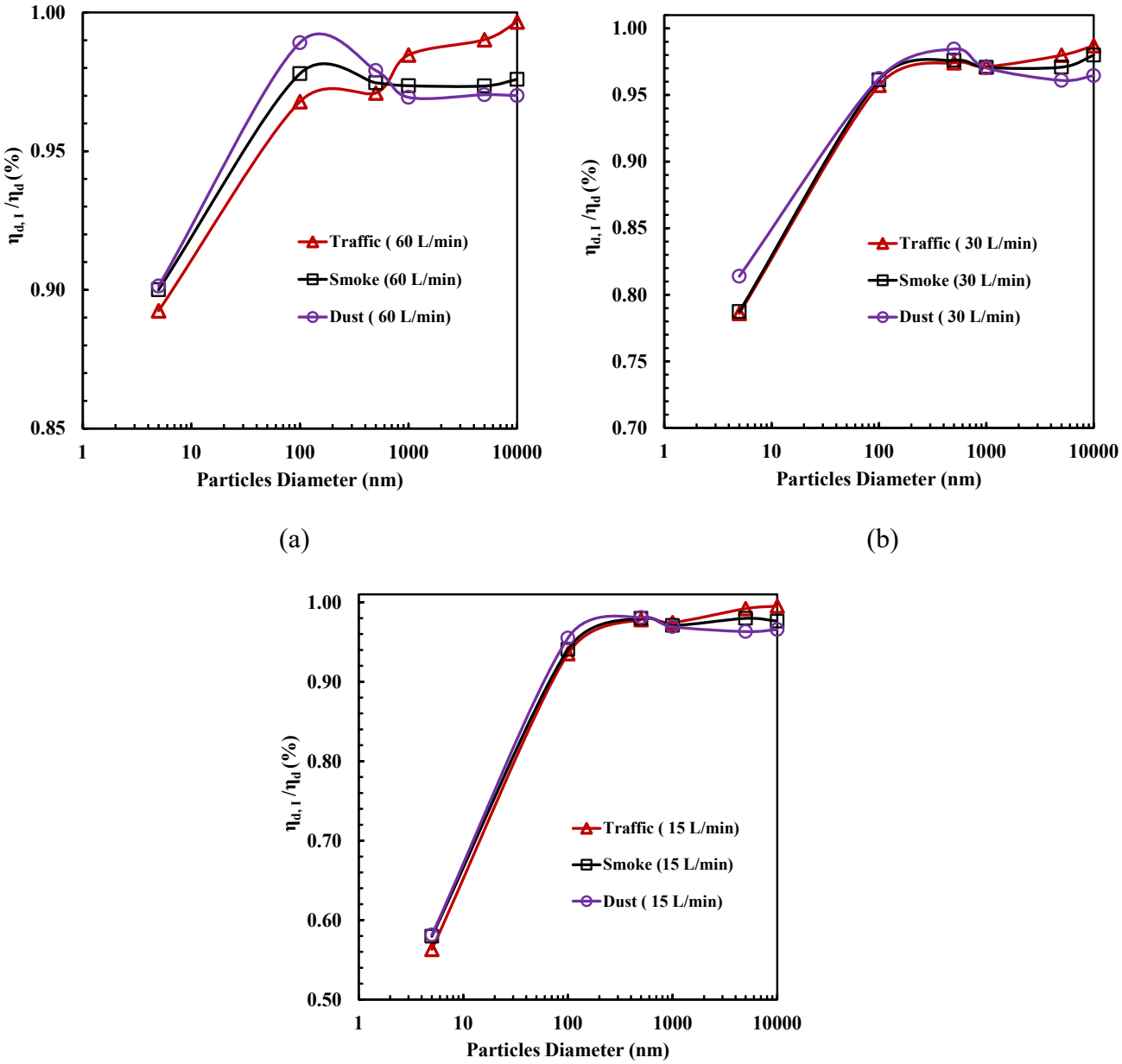

Figure 10. Contribution of the impaction mechanism on the deposition efficiency in the lung model for (a) Q_{in}=60 L/min; (b) Q_{in}=30 L/min and (c) Q_{in}=15 L/min.

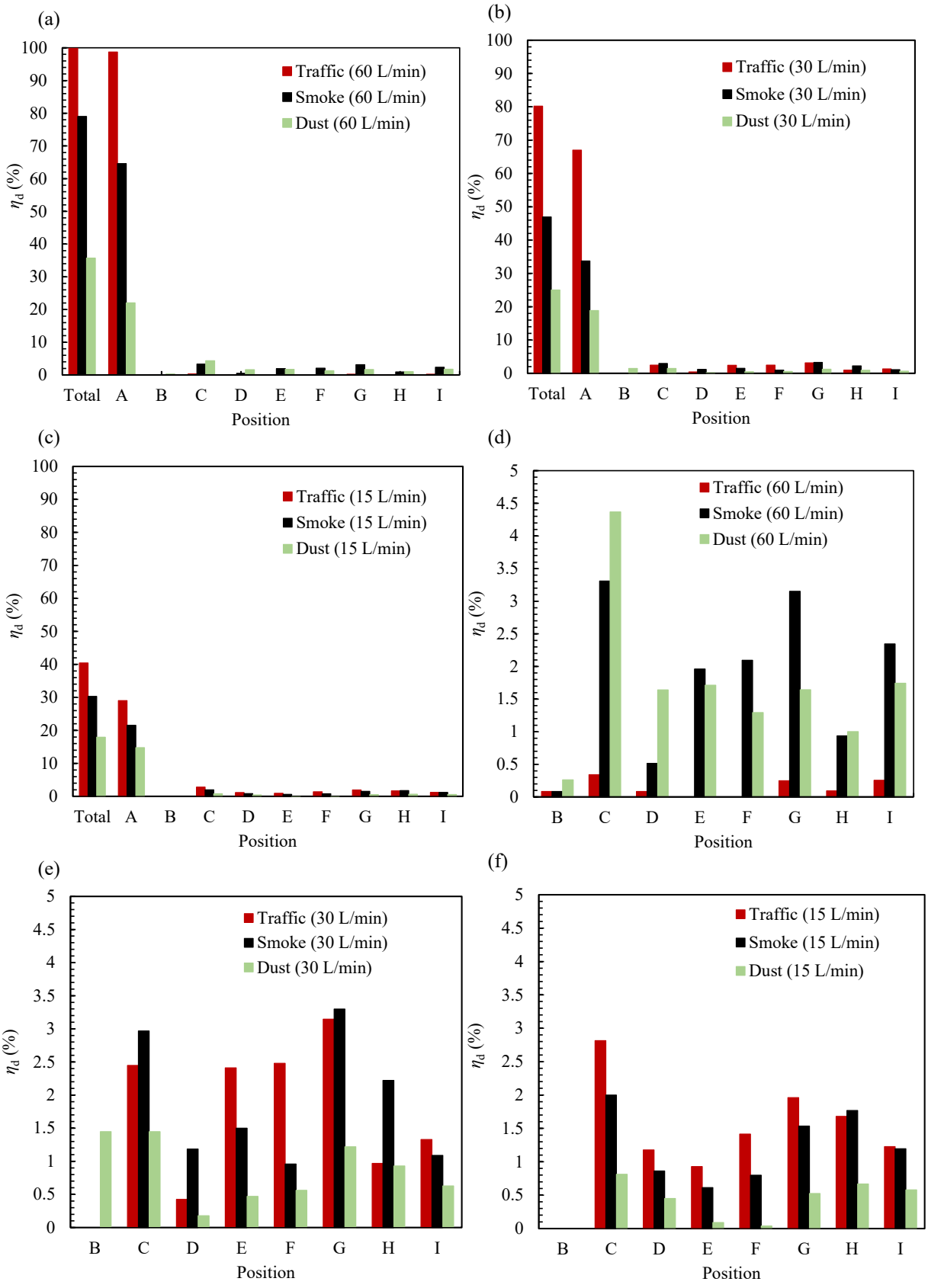

Figure 11. Deposition efficiencies of 10-μm particles at various parts of the lung indicated in Figure 1. (a) Q_{in}=60 L/min; (b) Q_{in}=30 L/min; (c) Q_{in}=15 L/min; (d) to (f) are the same as (a) to (c), respectively, except with smaller vertical axis scale for precise observation of deposition efficiencies at B to I.

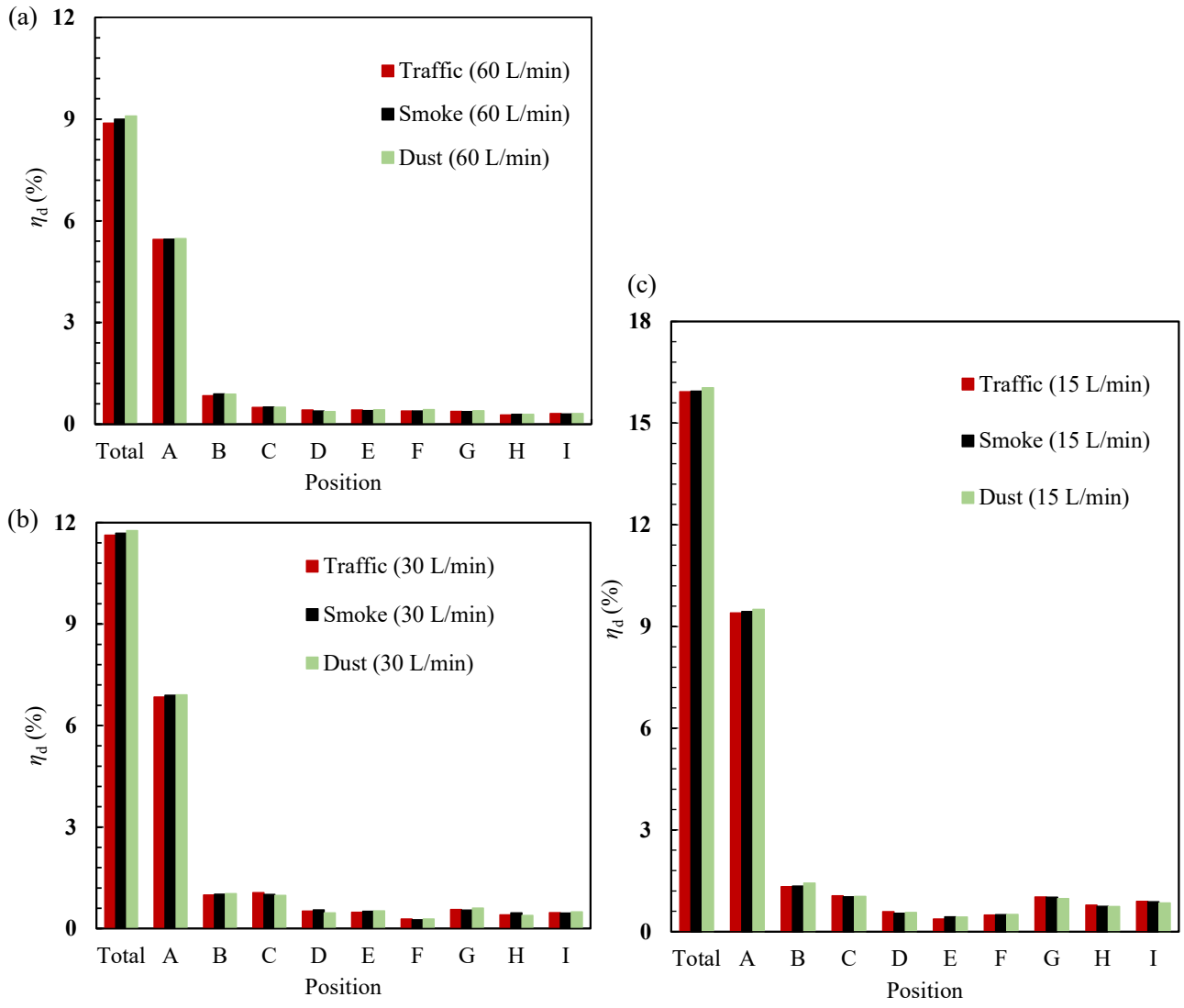

Figure 12. Deposition efficiencies of 5-nm particles at various parts of the lung indicated in Figure 1. (a) Q_{in}=60 L/min; (b) Q_{in}=30 L/min; (c) Q_{in}=15 L/min.

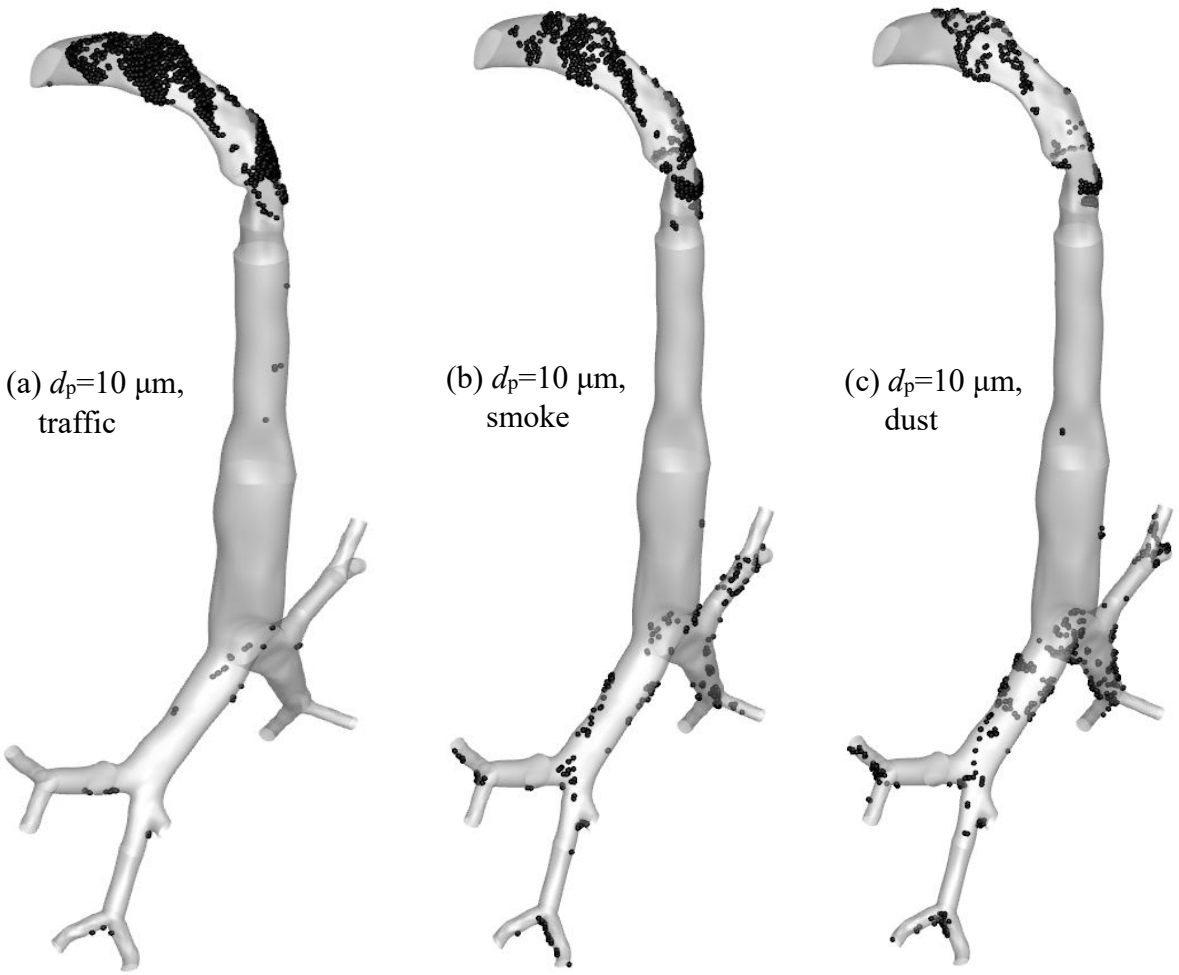

(a) d_p=10 μm, traffic

(b) d_p=10 μm, smoke

(c) d_p=10 μm, dust

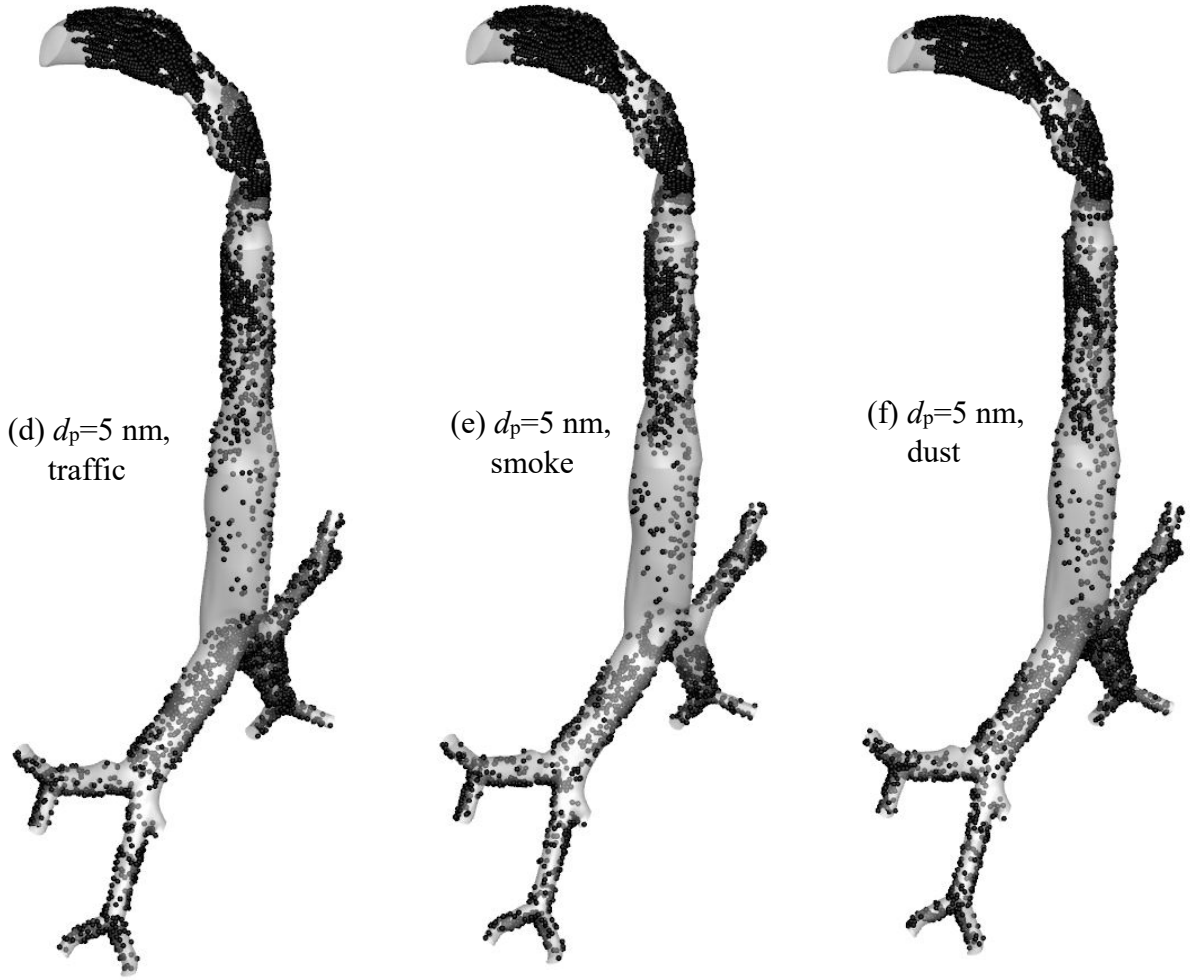

Figure 13. Distribution of deposited 10-μm and 5-nm particles in the human lung model at a flow rate of 60 L/min.

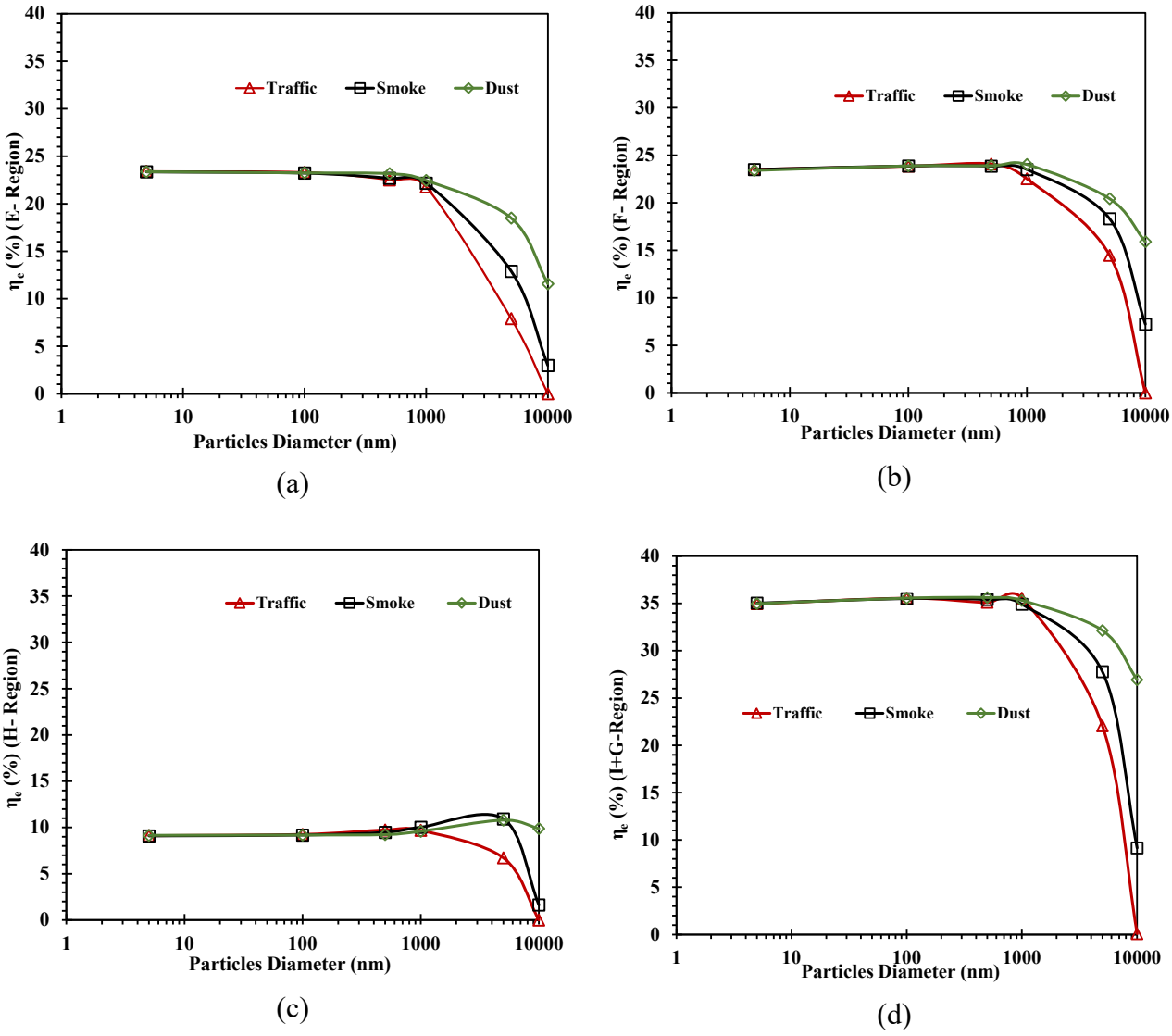

Figure 14. Escape rate (η_e) for 5 nm ≤ d_p ≤ 10 µm particles at a flow rate 60 L/min: (a) E region, (b) F region, (c) H region, and (d) I+G region (Figure 1 shows the description of a region).